# Transport properties of a quark-hadron Coulomb lattice in the cores of neutron stars

Xuesen Na[*] and Renxin Xu[†]

*Department of Astrophysics, School of Physics, Peking University, Beijing 100871, China*

Fridolin Weber[‡]

*Department of Physics, San Diego State University, 5500 Campanile Drive, San Diego, California 92182, USA*

Rodrigo Negreiros[§]

*Instituto de Física, Universidade Federal Fluminense, Avenida General Milton Tavares de Souza s/n, Gragoatá, Niterói 24210-346,*
*Brazil and Frankfurt Institute for Advanced Studies, Johann Wolfgang Goethe University,*
*Ruth-Moufang-Strasse 1, 60438 Frankfurt am Main, Germany*

Already more that 40 years ago, it has been suggested that because of the enormous mass densities in the cores of neutron stars, the hadrons in the centers of neutron stars may undergo a phase transition to deconfined quark matter. In this picture, neutron stars could contain cores made of pure (up, down, strange) quark matter which are surrounded by a mixed phase of quarks and hadrons. More than that, because of the competition between the Coulomb and the surface energies associated with the positively charged regions of nuclear matter and negatively charged regions of quark matter, the mixed phase may develop geometrical structures similarly to what is expected of the subnuclear liquid-gas phase transition. In this paper we restrict ourselves to considering the formation of rare phase blobs in the mixed quark-hadron phase. The influence of rare phase blobs on the thermal and transport properties of neutron star matter is investigated. The total specific heat $c_V$, thermal conductivity $\kappa$, and electron-blob bremsstrahlung neutrino emissivities $\epsilon_{\nu, \mathrm{BR}}$, of quark-hybrid matter are computed, and the results are compared with the associated thermal and transport properties of standard neutron star matter. Our results show that the contribution of rare phase blobs to the specific heat is negligibly small. This is different for the neutrino emissivity from electron-blob bremsstrahlung scattering, which turns out to be of the same order of magnitude as the total contributions from other bremsstrahlung processes for temperatures below about $10^8$ K.

## I. INTRODUCTION

Already many decades ago, it has been suggested that because of the extreme densities reached in the cores of neutron stars, neutrons and protons may transform to quark matter in the cores of such objects [1–6]. Quark matter could thus exist as a permanent component of matter in the ultradense centers of neutron stars (see Refs. [7–11] and references therein). If the dense interior of a neutron star is indeed converted to quark matter, it must be three-flavor quark matter since it has lower energy than two-flavor quark matter. And just as for the hyperon content of neutron stars, strangeness is not conserved on macroscopic time scales, which allows neutron stars to convert confined hadronic matter to three-flavor quark matter until equilibrium brings this process to a halt.

As first realized by Glendenning [12], the presence of quark matter enables the hadronic regions of the mixed phase to arrange to be more isospin symmetric than in the pure phase by transferring charge to the quark phase in equilibrium with it. The symmetry energy will be lowered thereby at only a small cost in rearranging the quark Fermi surfaces. The electrons play only a minor role when neutrality can be achieved among the baryon-charge carrying particles. The stellar implication of this charge rearrangement is that the mixed phase region of the star will have positively charged regions of nuclear matter and negatively charged regions of quark matter.

Because of the competition between the Coulomb and the surface energies associated with the positively charged regions of nuclear matter and negatively charged regions of quark matter, the mixed phase may develop geometrical structures (see Fig. 1), similarly as it is expected of the subnuclear liquid-gas phase transition [13–15]. This competition establishes the shapes, sizes, and spacings of the rare phase in the background of the other in order to minimize the lattice energy [7,11,12,16].

The change in energy accompanied by developing such geometrical structures is likely to be very small in comparison with the volume energy [12,17–19] and, thus, may not much affect the global properties of a neutron star. However, the geometrical structure of the mixed phase may

---

[*]naxuesen@pku.edu.cn, nxuesen@mail.sdsu.edu
[†]r.x.xu@pku.edu.cn
[‡]fweber@sciences.sdsu.edu
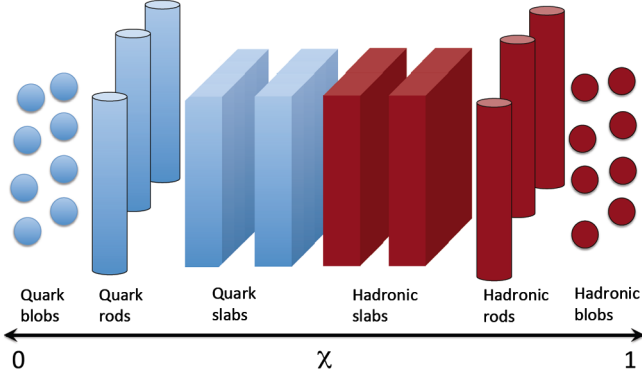[§]negreiros@fias.uni-frankfurt.de

FIG. 1 (color online). Schematic illustration of possible geometrical structures in the quark-hadron mixed phase of neutron stars. The structures may form because of the competition between the Coulomb and the surface energies associated with the positively charged regions of nuclear matter and negatively charged regions of quark matter.

be very important for irregularities (glitches) in the timing structure of pulsar spin-down as well as for the thermal and transport properties of neutron stars [8,12,17].

To calculate the neutrino-pair bremsstrahlung rates and thermal properties, we follow the method described in Refs. [20,21], which is commonly used for the calculation of the neutrino emissivity and thermal conductivity in the crusts of neutron stars. These authors considered contributions from electron-phonon scattering and Bragg diffraction (the static-lattice contribution). Furthermore, multiphonon processes and electron band structure effects are incorporated to obtain more realistic scattering rates and a better connection between the solid and the liquid gas phase. Instead of adopting the analytic fits provided in Refs. [20,21], here we recalculate the scattering rates from phonon sums using the method of Ref. [22]. There are two main reasons for this. The first being that, for the crust, the total ion charge is balanced by the total electron charge. This will be different for the mixed quark-hadron phase in the core of a neutron star, since electric charge neutrality is established between the electric charges of the rare phase, the dominant phase, and the leptons which are present in both the rare and the dominant phase. The simple relation $n_e = Z n_i$ between electron density and ion density used to derive the crustal fit formula in Refs. [20,21] can therefore not be used to study the quark-hadron Coulomb lattice structure in the core of a neutron star. The second reason concerns the electric charge numbers themselves. For mixed phase blobs, they can easily exceed $Z \sim 10^3$, as will be shown in Sec. II C. Charge numbers that high are obviously not reached in the crustal regimes of neutron stars [20], where there is usually no need to consider atomic nuclei with charges much larger than $Z > 56$.

The paper is organized as follows. In Sec. II, we briefly discuss the modeling of the mixed quark-hadron phase in the cores of neutron stars and the equations of state of

confined hadronic and quark matter used in this work. In Sec. III, we summarize the formalism for calculating the neutrino-pair bremsstrahlung emissivity and the thermal conductivity of rare phase blobs immersed in hadronic matter. The results are presented in Sec. IV.

## II. MODELING OF THE MIXED QUARK-HADRON PHASE IN NEUTRON STARS

### A. Hadronic matter

To compute the particle compositions of the cores of standard neutron stars, that is, neutron stars without deconfined quark degrees of freedom, we choose a relativistic Lagrangian of the following type [8,9]:

$$
\begin{aligned}
\mathcal{L} = \sum_B &\bar{\psi}_B [\gamma_\mu (i\partial^\mu - g_\omega \omega^\mu - g_\rho \vec{\tau} \cdot \vec{\rho}_\mu) \\
&- (m_N - g_\sigma \sigma)]\psi_B + \frac{1}{2}(\partial_\mu \sigma \partial^\mu \sigma - m_\sigma^2 \sigma^2) \\
&- \frac{1}{3}b_\sigma m_N (g_\sigma \sigma)^3 - \frac{1}{4}c_\sigma (g_\sigma \sigma)^4 - \frac{1}{4}\omega_{\mu\nu}\omega^{\mu\nu} \\
&+ \frac{1}{2}m_\omega^2 \omega_\mu \omega^\mu + \frac{1}{2}m_\rho^2 \vec{\rho}_\mu \cdot \vec{\rho}^\mu - \frac{1}{4}\vec{\rho}_{\mu\nu}\vec{\rho}^{\mu\nu} \\
&+ \sum_{\lambda = e^-, \mu^-} \bar{\psi}_\lambda (i\gamma_\mu \partial^\mu - m_\lambda)\psi_\lambda,
\end{aligned} \tag{1}
$$

where the sum over $B$ sums the baryon species listed in Table I. The sum over $\lambda$ accounts for the presence of relativistic electrons and muons in neutron star matter. Their masses are $m_e = 0.511$ MeV and $m_\mu = 105$ MeV. The quantities $g_\rho$, $g_\sigma$, and $g_\omega$ are meson-baryon coupling constants of $\sigma$, $\omega^\mu$, and $\vec{\rho}^\mu$ mesons. Nonlinear $\sigma$-meson self-interactions are taken into account in Eq. (1) via the terms proportional to $b_\sigma$ and $c_\sigma$. The quantities $\vec{\tau}$ and $\gamma^\mu$ denote isospin vectors and Dirac matrices, respectively, and $\partial^\mu \equiv \partial/\partial x_\mu$ [7,9]. We have solved the equations of motion for the baryon and meson fields, which follow from Eq. (1), in the framework of the relativistic mean-field approximation [7,9], where the fields $\sigma$, $\omega$, $\rho$ are approximated by their respective mean-field expectation values $\bar{\sigma} \equiv \langle \sigma \rangle$, $\bar{\omega} \equiv \langle \omega \rangle$, and $\bar{\rho} \equiv \langle \rho_{03} \rangle$. Two popular

TABLE I. Masses $m_B$, electric charges $Q_B$, spin $J_B$, and third component of isospin $I_B^3$ of the baryons $B$ included in the Lagrangian of Eq. (1) [8,9].

| $B$ | Symbol | $m_B$ (MeV) | $Q_B$ | $J_B$ | $I_B^3$ |
|---|---|---|---|---|---|
| $n$ | $m_n$ | 939 | 0 | 1/2 | $-1/2$ |
| $p$ | $m_p$ | 938 | 1 | 1/2 | 1/2 |
| $\Lambda$ | $m_\Lambda$ | 1115 | 0 | 0 | 0 |
| $\Sigma^+$ | $m_{\Sigma^+}$ | 1190 | 1 | 1 | 1 |
| $\Sigma^0$ | $m_{\Sigma^0}$ | 1190 | 0 | 1 | 0 |
| $\Sigma^-$ | $m_{\Sigma^-}$ | 1190 | $-1$ | 1 | $-1$ |
| $\Xi^0$ | $m_{\Xi^0}$ | 1315 | 0 | 1/2 | 0 |
| $\Xi^-$ | $m_{\Xi^-}$ | 1315 | $-1$ | 1/2 | $-1$ |

TABLE II.  Relativistic mean-field parametrizations used in this work.

| Coupling constants | Parametrizations | |
|---|---|---|
| | HV | G300 |
| $g_\sigma$ | 8.7982 | 9.1373 |
| $g_\omega$ | 9.1826 | 8.6324 |
| $g_\rho$ | 9.7145 | 8.3029 |
| $b_\sigma$ | 0.00414 | 0.003305 |
| $c_\sigma$ | 0.00716 | 0.01529 |

parametrizations labeled G300 and HV have been used [7,9,23–25]. Their parameters are summarized in Table II.

Neutron star matter is characterized by the conservation of two charges, electric and baryonic. This feature leads to the chemical equilibrium condition

$$\mu_i = B_i\mu_n - Q_i\mu_e, \tag{2}$$

where $\mu_n$ and $\mu_e$ are the chemical potentials of neutrons and electrons. The quantities $B_i$ and $Q_i$ stand for the baryon number and the electric charge of particles (mesons and baryons) of type $i$. Equation (2) greatly simplifies the mathematical analysis, since only knowledge of two independent chemical potentials $\mu_n$ and $\mu_e$ is necessary. The latter are given by

$$\begin{aligned} \mu_B &= g_\omega\bar{\omega} + g_\rho\rho_{03}^- I_B^3 + \sqrt{k_B^2 + m_B^{*2}}, \\ \mu_\lambda &= \sqrt{k_\lambda^2 + m_\lambda^2}, \end{aligned} \tag{3}$$

where $m_B^* = m_B - g_{\sigma B}\bar{\sigma}$ denote the effective medium-modified baryon masses, $k_B$ and $k_\lambda$ are the Fermi momenta of baryons and leptons, respectively, and $\hat{I}_B^3$ is the third component of the isospin vector of a baryon of type $B$. Finally, aside from chemical equilibrium, the condition of electric charge neutrality is also of critical importance for the composition of neutron star matter. It is given by

$$\sum_B Q_i(2J_B + 1)\frac{k_B^3}{6\pi^2} - \sum_\lambda \frac{k_\lambda^3}{3\pi^2} = 0. \tag{4}$$

Figure 2 shows the baryon-lepton compositions of neutron star matter computed from Eq. (1) for the relativistic mean-field approximation. The quantity $\rho_i$ in Fig. 2 stands for the individual number densities of baryons,

$$\rho_B = (2J_B + 1)k_B^3/3\pi^3, \tag{5}$$

whose total number density is given by

$$\rho_b \equiv \sum_B \rho_B. \tag{6}$$

The individual number densities of electrons and muons ($i = e^-, \mu^-$) are given by
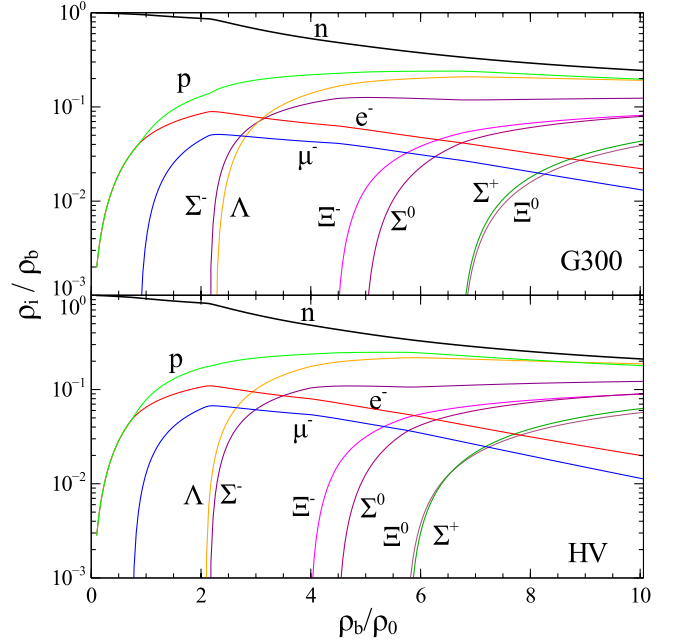
$$\rho_i = 2k_i^3/3\pi^3. \tag{7}$$



FIG. 2 (color online).  Sample baryon-lepton compositions $\rho_i/\rho_b$ of neutron star matter computed for G300 (upper panel) and HV (lower panel).

The total energy density and pressure of the matter shown in Fig. 2 follow from

$$\begin{aligned} \epsilon_H &= \frac{1}{3}bm_N(g_\sigma\bar{\sigma})^3 + \frac{1}{4}c(g_\sigma\bar{\sigma})^4 + \frac{1}{2}(m_\sigma\bar{\sigma})^2 + \frac{1}{2}(m_\omega\bar{\omega})^2 \\ &+ \frac{1}{2}(m_\rho\bar{\rho})^2 + \sum_B \frac{1}{\pi^2}\int_0^{k_B} k^2 dk\sqrt{k^2 + m_B^{*2}} \\ &+ \sum_\lambda \frac{1}{\pi^2}\int_0^{k_\lambda} k^2 dk\sqrt{k^2 + m_\lambda^2}, \end{aligned} \tag{8}$$

and

$$\begin{aligned} p_H &= -\frac{1}{3}bm_N(g_\sigma\bar{\sigma})^3 - \frac{1}{4}c(g_\sigma\bar{\sigma})^4 - \frac{1}{2}(m_\sigma\bar{\sigma})^2 \\ &+ \frac{1}{2}(m_\omega\bar{\omega})^2 + \frac{1}{2}(m_\rho\bar{\rho})^2 \\ &+ \sum_B \frac{1}{\pi^2}\int_0^{k_B} k^2 dk\sqrt{k^2 + m_B^{*2}} \\ &+ \sum_\lambda \frac{1}{\pi^2}\int_0^{k_\lambda} k^2 dk\sqrt{k^2 + m_\lambda^2}. \end{aligned} \tag{9}$$

### B. Quark matter

To model quark matter, we use the bag model. Up ($u$) and down ($d$) quarks are treated as massless particles while the strange quark ($s$) mass is assigned a value of $m_s = 200$ MeV. First-order perturbative corrections in the strong interaction coupling constant $\alpha$ are taken into account [10,26–28]. The Landau potentials of up and down quarks are then given by

$$\Omega_u = -\frac{\mu_u^4}{4\pi^2}\left(1 - \frac{2\alpha}{\pi}\right), \qquad (10)$$

$$\Omega_d = -\frac{\mu_d^4}{4\pi^2}\left(1 - \frac{2\alpha}{\pi}\right), \qquad (11)$$

while for strange quarks we have

$$\begin{aligned}
\Omega_s = -\frac{1}{4\pi^2}&\left\{\mu_s\sqrt{\mu_s^2 - m_s^2}\left(\mu_s^2 - \frac{5}{2}m_s^2\right)\right.\\
&+ \frac{3}{2}m_s^4 f(\mu_s, m_s) - \frac{2\alpha}{\pi}\left[3(\mu_s\sqrt{\mu_s^2 - m_s^2}\right.\\
&- m_s^2 f(\mu_s, m_s))^2 - 2(\mu_s^2 - m_s^2)^2 + 3m_s^4\ln^2\frac{m_s}{\mu_s}\\
&\left.\left.+ 6\ln\frac{\sigma}{\mu_s}\left(\mu_s m_s^2\sqrt{\mu_s^2 - m_s^2} - m_s^4 f(\mu_s, m_s)\right)\right]\right\},
\end{aligned}$$
$$(12)$$

where $f(\mu, m) \equiv \ln((\mu + \sqrt{\mu^2 - m^2})/m)$, and $\sigma$ is a renormalization constant whose value is of the order of the chemical potentials [28]. In this article we take $\sigma = 300$ MeV. The Landau potentials of electrons and muons are given by

$$\Omega_e = -\frac{\mu_e^4}{12\pi^2}, \qquad (13)$$

$$\begin{aligned}
\Omega_\mu = -\frac{1}{4\pi^2}&\left(\mu_\mu\sqrt{\mu_\mu^2 - m_\mu^2}\left(\mu_\mu^2 - \frac{5}{2}m_\mu^2\right)\right.\\
&\left.+ \frac{3}{2}m_\mu^4 \ln\left(\frac{\mu_\mu + \sqrt{\mu_\mu^2 + m_\mu^2}}{m_\mu}\right)\right). 
\end{aligned}$$
$$(14)$$

The condition of chemical equilibrium leads to

$$\mu_d = \mu_s = \mu_u + \mu_e = \mu_u + \mu_\mu. \qquad (15)$$

The partial baryon number densities of the particles are obtained from ($i = u, d, s, e^-, \mu^-$)

$$\rho_i = -\partial\Omega_i/\partial\mu_i, \qquad (16)$$

and the total energy density and pressure of quark matter follows from

$$\epsilon_Q = \sum_i(\Omega_i + \mu_i\rho_i) + B, \qquad (17)$$

and

$$p_Q = -B - \sum_i \Omega_i, \qquad (18)$$

where $B$ denotes the bag constant. For $\alpha, m_s \to 0$ one recovers from Eqs. (17) and (18) the standard equation of state of a massless relativistic quark gas, $P = (\epsilon - 4B)/3$.

## C. Geometric structures in the mixed quark-hadron phase

To determine the possible geometric structures in the mixed phase of quarks and hadrons, we use the Gibbs condition

$$p_H(\mu_n, \mu_e, \{\phi\}) = p_Q(\mu_n, \mu_e) \qquad (19)$$

for phase equilibrium between hadronic matter and quark matter [12]. The quantity $\{\phi\}$ in Eq. (19) stands collectively for the field variables $(\bar{\sigma}, \bar{\omega}, \bar{\rho})$ and Fermi momenta $(k_B, k_\lambda)$ that characterize a solution to the equations of confined hadronic matter. We use the symbol $\chi \equiv V_Q/V$ to denote the volume proportion of quark matter $V_Q$ in the unknown volume $V$. By definition, $\chi$ then varies between 0 and 1 depending on how much confined hadronic matter has been converted to quark matter. Equation (19) is to be supplemented with the condition of baryon charge conservation and electric charge conservation. The global conservation of baryon charge is expressed as

$$\rho_b = \chi\rho_Q(\mu_n, \mu_e) + (1 - \chi)\rho_H(\mu_n, \mu_e, \{\phi\}), \qquad (20)$$

and the global neutrality of electric charge is given by

$$0 = \chi q_Q(\mu_n, \mu_e) + (1 - \chi)q_H(\mu_n, \mu_e, \{\phi\}). \qquad (21)$$

In Figs. 3 and 4 we show sample compositions of neutron star matter computed for four different parameter sets (see Table III) which allow for the presence of a mixed phase of quark and hadrons. One sees that the $\Sigma^-$ population is strongly suppressed in the mixed quark-hadron phase, since the hadronic phase carries a net positive
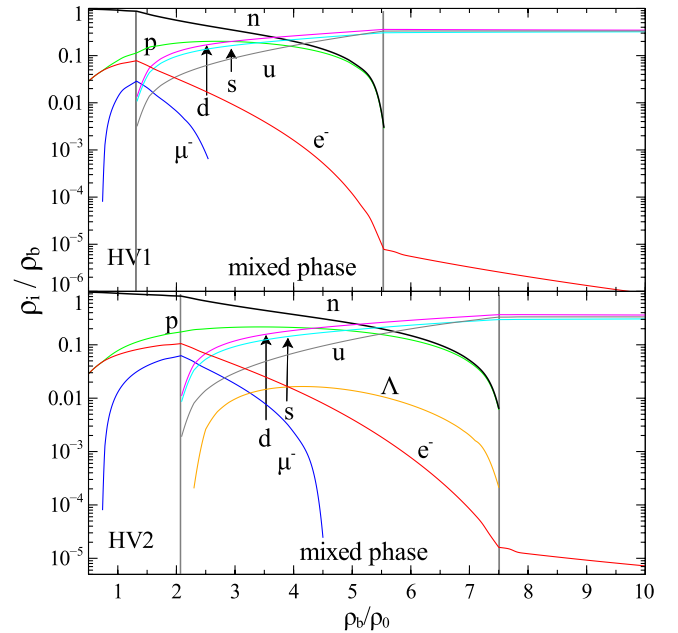


FIG. 3 (color online). Particle composition $\rho_i/\rho_b$ of neutron star matter with mixed quark-hadron phase. The parameter sets are HV1 and HV2 (see Table III).
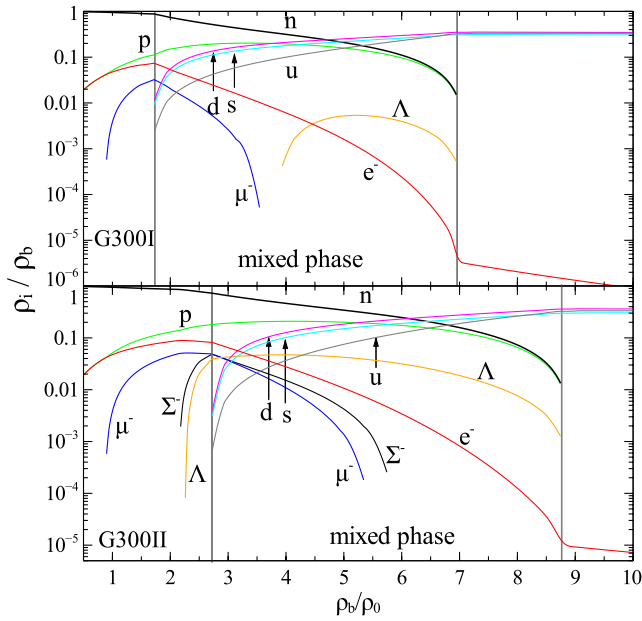
FIG. 4 (color online).   Same as Fig. 3 but for parameter sets G300I and G300II (see Table III).

charge which disfavors the presence of the $\Sigma^-$. In contrast to this, the $\Lambda$ particle is electrically neutral so that its presence is not disfavored by electric charge reasons. As to the population computed for parametrization G300II, shown in Fig. 4 (bottom panel), the threshold of the $\Sigma^-$ is reached before quark deconfinement sets in. As soon as quark deconfinement occurs, however, the $\Sigma^-$ population drops quickly with density while the $\Lambda$ population remains relatively unaffected, enabling hadronic matter to be positively charged and quark matter to be negatively charged.

As can also be seen from Figs. 3 and 4, the mixed quark-hadron phases obtained for the G300 parametrizations exist over a broader density range than HV. This feature has its origin in the density dependence of $\mu_n$, which increases faster with density for the HV1 and HV2 models, rendering these equations of state stiffer than the G300I and G300II models for the equation of state.

A larger value for the bag constant $B$ reduces the pressure of the quark phase, which too leads to a broader mixed phase region. It also follows from Figs. 3 and 4 that the number of electrons as well as the number of muons drops quickly with density, since charge neutrality is achieved

TABLE III.   Parameter sets of the quark-hybrid star models of this work. $B$ denotes the bag constant, $\alpha$ is the strong interaction coupling constant.

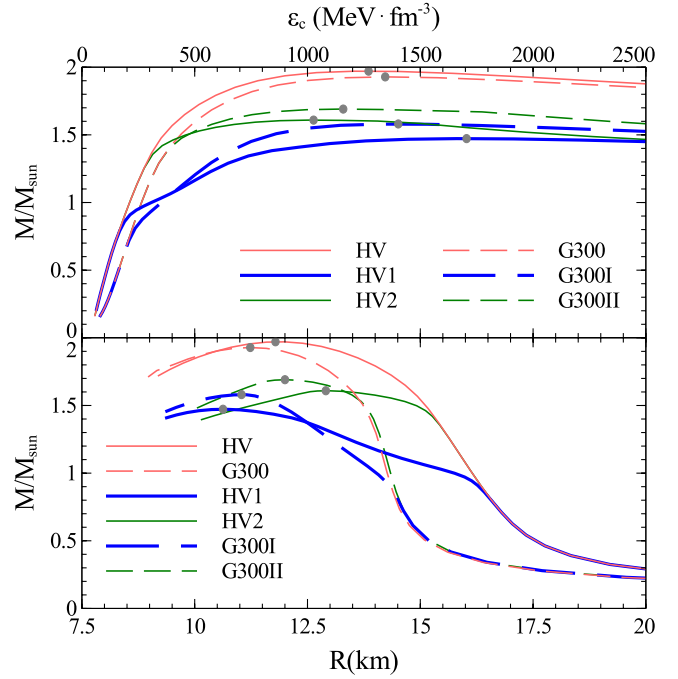| Label | Hadronic phase | Quark phase |
|---|---|---|
| HV1 | HV | $B = 110$ MeV fm$^{-3}$, $\alpha = 0.2$ |
| HV2 | HV | $B = 160$ MeV fm$^{-3}$, $\alpha = 0.1$ |
| G300I | G300 | $B = 110$ MeV fm$^{-3}$, $\alpha = 0.2$ |
| G300II | G300 | $B = 160$ MeV fm$^{-3}$, $\alpha = 0.1$ |



FIG. 5 (color online).   Mass-central density (top panel) and mass-radius (bottom panel) relationships of neutron stars for the parameter sets listed in Table III. The solid dots denote the most massive neutron star model of each sequence.

chiefly among the quarks themselves. For values of the strong interaction coupling constant $\alpha \gtrsim 0.25$ electrons disappear from the matter and positrons tend to emerge in the mixed phase. We therefore consider only $\alpha \lesssim 0.2$.

In Fig. 5 we show the masses of neutron stars, whose compositions are given in Figs. 3 and 4. The underlying equations of state are given in Eqs. (8), (9), (17), and (18), and the parameter sets are listed in Table III. The Baym-Pethick-Sutherland model for the equation of state has been used to model the crusts of these neutron stars [29]. The maximum masses of the quark-hybrid stars computed for HV1 and HV2 are $1.47M_\odot$ and $1.61M_\odot$, respectively. For G300I and G300II we obtain maximum masses of $1.58M_\odot$ and $1.69M_\odot$, respectively. These values are too low to accommodate the recently discovered heavy pulsar PSR J1614-2230, whose mass is $M = 1.97 \pm 0.04M_\odot$ [30]. One possible explanation could be that the high rotation rate of this neutron star prevents the hadrons in the core of this neutron star from transforming to quark-hadron matter. This neutron star could thus be made entirely of confined hadronic matter, whose equation of state is stiffer than the equation of state of quark-hybrid matter supporting high-mass neutron stars. As found in Ref. [31], massive ($\sim 2M_\odot$) nonrotating neutron stars with extended regions of deconfined quarks and hadrons are comfortably obtained in the framework of the nonlocal SU(3) Nambu-Jona-Lasinio model. This model is not considered in this paper, however, since our results are largely independent of the particular microscopic many-body

model chosen to determine the equation of state of bulk quark-hadron matter.

As pointed out in Refs. [7,12] the isospin restoring force can exploit degrees of freedom made available by relaxing the requirement of strict local charge neutrality to neutrality on larger scales and form a positively charged hadronic matter region with lower isospin asymmetry energy and a negatively charged quark matter region. The competition between the Coulomb interaction and the surface energy will result in a crystalline lattice of the rare phase in the dominant phase. The size and spacing of the crystalline lattice is determined by minimizing the total energy. The situation is similar to the atomic nuclei immersed in a relativistic electron gas in the crusts of neutron stars.

Depending on density, the embedding of the rare phase in the dominant phase can lead to different geometric structures, including spherical blobs, rods, and slabs. In what follows, we restrict ourselves to the discussion of spherical blobs. For an electrically charge neutral Wigner-Seitz cell, with spherical blob of radius $r_b$, the Coulomb and surface energy density can be expressed as

$$\epsilon_C = 2\pi\alpha_e[q_H(\chi) - q_Q(\chi)]^2 r_b^2 \chi f_3(x), \qquad (22)$$

$$\epsilon_S = 3\chi\sigma(\chi)/r_b, \qquad (23)$$

where $\alpha_e = 1/137$ is the fine structure constant, $x = \min(\chi, 1 - \chi)$ is the volume fraction of rare phase, and $f_3(x) = (x - 3x^{1/3} + 2)/5$ is the function $f_d(x)$ for $d = 3$, which arises from calculating the electrostatic binding energy of the cell [7]. Due to theoretical difficulties it is very hard to estimate the surface tension $\sigma$. Here we follow Ref. [7] and take a gross approximation expression for the surface tension first proposed by Gibbs [32], where the surface energy is proportional to the difference of the energy densities of the two phases,

$$\sigma(\chi) = \eta L[\epsilon_Q(\chi) - \epsilon_H(\chi)], \qquad (24)$$

where $\eta$ should be on the order of $\eta \sim \mathcal{O}(1)$, and we take $L = 1$ fm. Three different values for the constant $\eta$ (i.e., 0.5, 1, and 2) are used in our calculations to investigate the effects caused by uncertainties in the value of the surface tension.

Since $\epsilon_C \propto r_b^2$ and $\epsilon_S \propto r_b^{-1}$, it is possible to minimize the total energy $\epsilon_C + \epsilon_S$ at fixed $\chi$ which leads to an equilibrium radius of the rare phase of blobs inside of Wigner-Seitz cells,

$$r_b = \left(\frac{3\sigma(\chi)}{4\pi\alpha_e[q_H(\chi) - q_Q(\chi)]^2 f_3(x)}\right). \qquad (25)$$

The radii of spherical blobs of the rare phase $r_b$ and the radii of Wigner-Seitz cells $a$ as a function of the quark volume fraction $\chi$ are shown in Fig. 6. The radii of spherical blobs is in the range of 10 to 30 fm. To compare our situation to the crust we also calculate the charge $Z$ and mass number $A = m_b/m_u$ of the rare phase blobs, with $m_b$
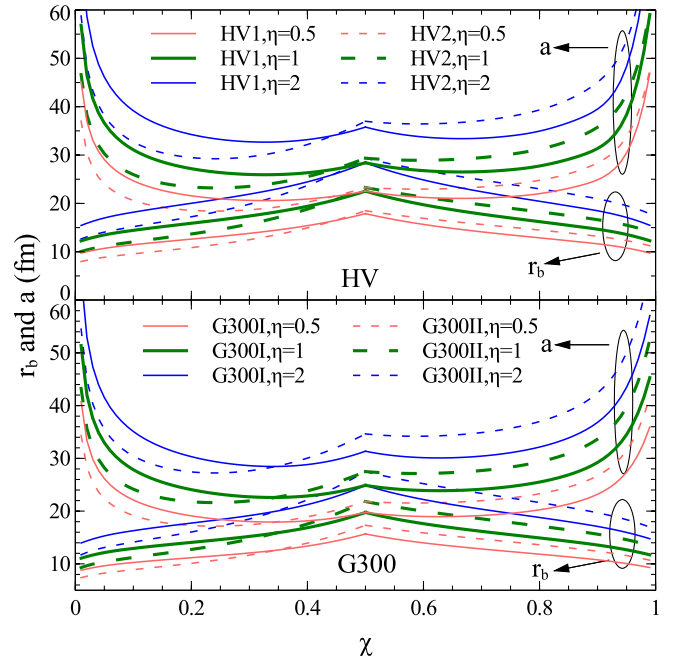


FIG. 6 (color online). Radii of spherical blobs $r_b$ and Wigner-Seitz cells $a$ as a function of quark volume fraction $\chi$ for different surface tensions $\eta$ and parameter sets (Table III) of the hadronic lagrangian.

being the blob mass. In addition we define an effective electric charge number given by

$$Z_{eff} = \frac{n_e}{n_b}, \qquad (26)$$

where $n_b$ is the number density of the spherical blobs. The values of $Z$, $A$, and $Z_{eff}$ as a function of the quark volume
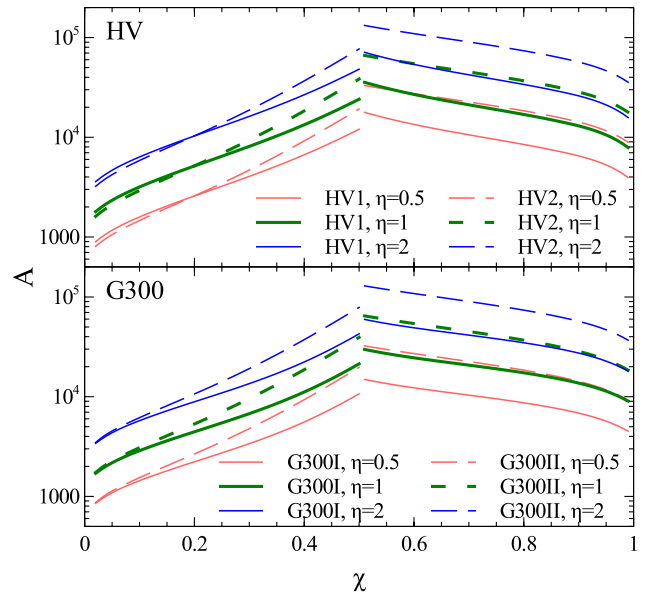


FIG. 7 (color online). Mass number $A = m_b/m_u$ of spherical blobs of rare phase as a function of quark volume fraction $\chi$.
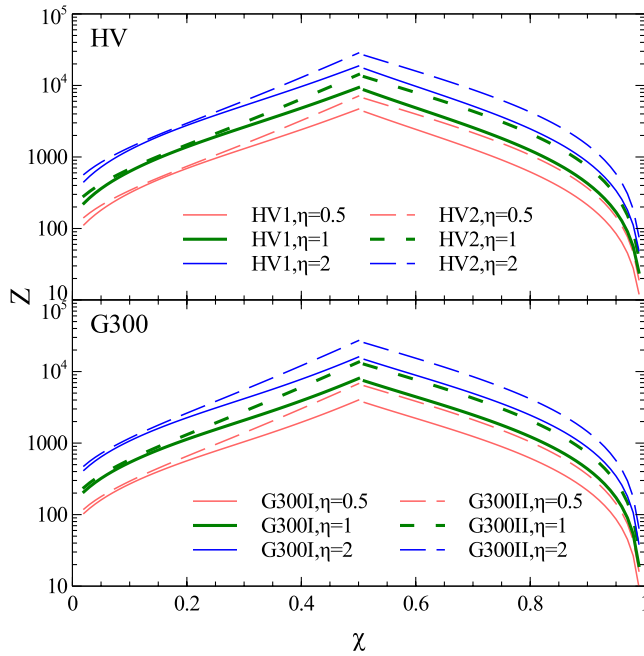
FIG. 8 (color online). Electric charge number $Z$ of spherical blobs of rare phase as a function of quark volume fraction $\chi$.

fraction are shown in Figs. 7–9. As can be seen, the charge and mass numbers are typically one to two orders of magnitude greater than that of the heaviest stable nuclei, but due to a dramatic drop in electron density the value of $Z_{\rm eff}$ can fall near and below $Z_{\rm eff} \sim 10$ as $\chi \to 1$. The discontinuities of the curves in Fig. 7 at $\chi = 0.5$ are due to
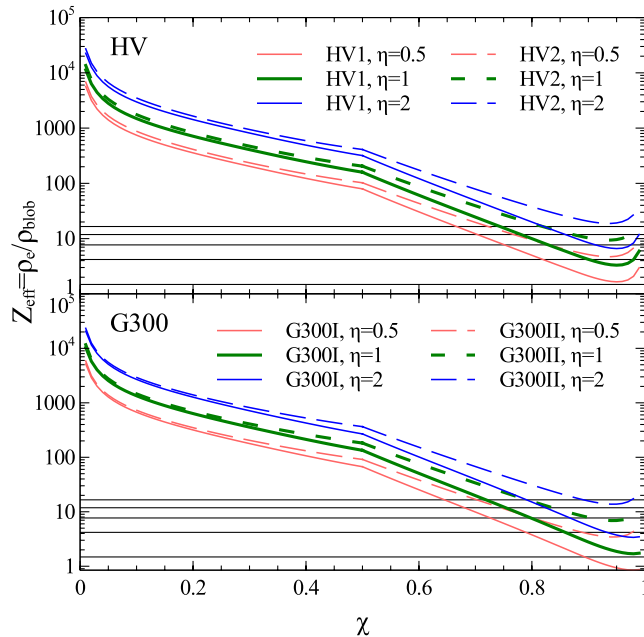


FIG. 9 (color online). Effective charge number $Z_{\rm eff}$ of spherical blobs of rare phase as a function of quark volume fraction $\chi$. The five horizontal lines at the bottom of each panel correspond to $Z_{\rm eff,min}^{(n)}$ for $n = 1, 2, 3, 4, 5$ (see Sec. III B).

the differences in the hadronic and quark phase densities at $\chi = 0.5$. It is also worth noting that near the edges of the mixed phase region ($\chi \to 0, 1$) the volume density of blobs $n_b = 3x/(4\pi r_b^3)$ vanishes, but since $f_3(0) = 2/5$, the blob radius $r_b$ approaches a constant $r_b \to r_b(x = 0)$. Therefore $Z_{\rm eff} = n_e/n_b$ diverges at the edges of the mixed phase region.

## III. THERMAL AND TRANSPORT PROPERTIES OF QUARK-HADRON PHASE

Next, we turn our interest to the calculation of the thermal and transport properties of a mixed phase of quarks and hadrons. Knowledge of these properties is of key importance in order to carry out thermal evolution simulations of neutron stars with hypothetical quark-hadron cores and to determine possible astrophysical signatures hinting at the existence of such matter inside of neutron stars. Our focus here is on exploring the impact of rare phase blobs on the following properties: specific heat $c_V$, neutrino emissivity $\epsilon_\nu$, and thermal conductivity $\kappa$.

From the outset, one might expect that because of the geometric structures in the mixed phase, new degrees of freedom are introduced to the system, which may store additional thermal energy and hence would increase the specific heat. Due to the scattering of degenerate electrons and rare phase blobs in the mixed phase, there will also be an additional contribution to the neutrino bremsstrahlung and an additional microscopic entropy production rate which reduces the total thermal conductivity.

### A. Basic physical quantities

We first introduce some of the basic physical quantities and functions used in the calculation of the thermal and transport properties of the quark-hadron phase. The state of the mixed phase with rare phase blobs is determined by the ion-coupling parameter [20],

$$\Gamma = \frac{Z^2 e^2}{a k_B T}, \qquad (27)$$

where $a = (3/(4\pi n_b))^{1/3}$ is the Wigner-Seitz cell radius, which is related to the spherical blob radius by $x = (r_b/a)^3$. The quantity $\Gamma_m = 172$ corresponds to the melting point below which a classical one-component Coulomb crystal ($\Gamma < \Gamma_m$) becomes a Coulomb liquid ($1 < \Gamma < \Gamma_m$) [33]. Therefore the melting temperature is given by $T_m = Z^2 e^2/(a k_B \Gamma_m)$. Another important quantity is the plasma temperature,

$$T_p = \frac{\hbar \omega_p}{k_B}, \qquad (28)$$

where $\omega_p = (4\pi Z^2 e^2 n_b/m_b)^{1/2}$ denotes the plasma frequency of the spherical blobs, with $m_b$ the mass of the spherical blobs. For later, it is convenient to introduce the temperature in units of the plasma temperature,

$t_p = T/T_p$. For temperatures $t_p \lesssim 1/8$ the vibrations of a Coulomb crystal must be treated quantum mechanically [20].

Besides the Coulomb interaction, there are three effects which must be taken into account to describe the interaction between electrons and rare phase blobs. These are the screening of electrons, the shape of the blob, and the effect of thermal vibrations. The Fourier transform of the effective electron-blob interaction is given by [20]

$$V(q) = \frac{4\pi e \rho_Z F(q)}{q^2 \epsilon(q)} e^{-W(q)}, \qquad (29)$$

where $\rho_Z$ is the blob charge per unit volume $\rho_Z = \chi q_Q$ for $\chi < 1/2$, and $\rho_Z = (1 - \chi)q_H$ for $\chi > 1/2$. The quantity $\epsilon(q)$ in Eq. (29) is the static longitudinal dielectric factor adopted from Ref. [34], and $F(q)$ is the form factor of a blob. For simplicity, we assume a uniform distribution of the electric charge in the rare phase and use $F(q) = (3/(qr)^3)[\sin(qr) - qr\cos(qr)]$ [20].

Thermal vibrations of rare phase blobs are taken into account via the Debye-Waller factor,

$$W(q) = \frac{\hbar q^2}{4m_b} \left\langle \frac{\coth(\hbar \omega_s/(2k_B T))}{\omega_s} \right\rangle_{\text{ph}}, \qquad (30)$$

where $\omega_s$ is the phonon frequency. Here $\langle \ldots \rangle_{\text{ph}}$ denotes the average over the phonon wave vectors and polarizations. Throughout this article, we use the method of Ref. [22] to compute phonon sums. It is assumed that there are three polarizations of phonons: two transverse modes with linear dispersion relations $\omega_k^{(t,i)} = a_i k$ ($i = 1, 2$), and one longitudinal mode which is determined through Kohn's sum rule $\omega_{t,1}^2 + \omega_{t,2}^2 + \omega_l^2 = \omega_p^2$, where $\omega_p$ denotes the plasma frequency. The two parameters $a_1$ and $a_2$ are determined by fitting the frequency moments $u_n \equiv \langle \omega^n \rangle_{\text{ph}}$ of the specified lattice type. For a bcc lattice, the frequency moments $u_{-1} = 2.7990$ and $u_{-2} = 12.998$ are well known [35] and are used to obtain $a_1 = 0.58273$, $a_2 = 0.32296$. These parameters also produce first and fourth moments: $\mu_1 = 0.51106$, $\mu_4 = 0.201946$ which are quite close to the exact values of $\mu_1 = 0.51139$ and $\mu_4 = 0.203076$ [35]. In the special case of the Debye-Waller factor, the phonon sum can be fitted very well by the following analytic formula [36]:

$$W(q) = \frac{\alpha_0}{2} \left(\frac{q}{2k_F}\right)^2 \left(\frac{1}{2} u_{-1} e^{-9.1t_p} + t_p u_{-2}\right), \qquad (31)$$

where $k_F$ is electron Fermi wave number and $\alpha_0$ is a constant given in Ref. [20]. The latter can be rewritten as

$$\tilde{\alpha} \equiv \frac{\alpha_0}{2} = \frac{3^{2/3} \pi^{5/6} \hbar^{1/2}}{\alpha_e^{1/2} c^{1/2}} \frac{n_e^{2/3}}{Z m_b^{1/2} n_b^{1/2}}. \qquad (32)$$

With the help of Eq. (32) the Debye-Waller factor can be written as $W(y^2 \tilde{\alpha}, t_p)$, where $y = q/(2k_F)$.

### B. Neutrino bremsstrahlung emissivity

Next we turn to the calculation of the scattering of electrons off the rare phase blobs (that is, electron-blob bremsstrahlung), which leads to the generation of neutrino-antineutrino pairs according to the reaction $e^- + (Z, A) \rightarrow e^- + (Z, A) + \nu + \bar{\nu}$. The associated neutrino bremsstrahlung emissivity can be written as [37]

$$\epsilon_\nu = \frac{8\pi G_F^2 Z^2 e^4 C_+^2}{567 \hbar^9 c^8} (k_B T)^6 n_b L, \qquad (33)$$

where $n_b$ is the number density of the rare phase blobs and $G_F = 1.436 \times 10^{-49}$ erg cm$^3$ is the Fermi weak coupling constant $C_+^2 \approx 1.675$ [20], and $L$ is a dimensionless function given by

$$L = L_{\text{ph}} + L_{\text{sl}} \quad \text{or} \quad L = L_{\text{liq}}, \qquad (34)$$

where $L_{\text{ph}}$ accounts for the scattering of electrons off the phonons of the Coulomb crystal of rare phase blobs, $L_{\text{sl}}$ accounts for Bragg scattering between electrons and the static Coulomb crystal lattice, and $L_{\text{liq}}$ is for the liquid phase. In the liquid phase the general expression is obtained through a variational approach in Born approximation [37–39],

$$L_{\text{liq}} = \int_0^1 dy \frac{S(q)|F(q)|^2}{y|\epsilon(q)|^2} \left(1 + \frac{2y^2}{1 - y^2} \ln y\right), \qquad (35)$$

where $y = q/(2k_F)$. We follow Ref. [20] for the choice of the ion-ion structure factor $S(q)$, which was fitted in Refs. [40,41]. For a solid phase the phonon contribution is mainly given by umklapp processes, which in Born approximation can be written as [20,39]

$$L_{\text{ph}} = \int_{y_0}^1 dy \frac{S_{\text{eff}}(y^2 \tilde{\alpha}, t_p)|F(y)|^2}{y|\epsilon(y)|^2} \left(1 + \frac{2y^2}{1 - y^2} \ln y\right), \qquad (36)$$

where the lower integration limit $y_0 = (4Z_{\text{eff}})^{-1/3}$ excludes the low-momentum transfers in which the umklapp processes are forbidden [20], and the effective static structure factor $S_{\text{eff}}$ is obtained from the summation of multiphonon diagrams [20,42]. For the parameter sets chosen in this calculation we always have $Z_{\text{eff}} > 1/4$ so that $y_0 < 1$. $S_{\text{eff}}$ can be written in terms of a rapidly decreasing integral [20],

$$S_{\text{eff}}(y^2 \tilde{\alpha}, t_p) = 189 \left(\frac{2}{\pi}\right)^5 e^{-2W(y^2 \tilde{\alpha}, t_p)}$$
$$\times \int_0^\infty d\xi \frac{1 - 40\xi^2 + 80\xi^4}{(1 + 4\xi^2)^5 \cosh^2(\pi \xi)}$$
$$\times (e^{\Phi(\xi, y^2 \tilde{\alpha}, t_p)} - 1), \qquad (37)$$

where

$$\Phi(\xi, x, t_p) \equiv x \left\langle \frac{\cos(\frac{\xi \omega}{t_p})}{\omega \sinh(\frac{\omega}{2t_p})} \right\rangle_{\text{ph}}, \qquad (38)$$

with $\omega \equiv \omega_s/\omega_p$ denoting the phonon frequency in units of the plasma frequency. Similarly to the analysis in Ref. [20], there exist approximate expressions for $S_{\rm eff}$ for the limiting cases where $t_p \ll 1$ and $t_p \gg 1$, which is discussed next. For this purpose, we write the $x$-independent part of $\Phi(\xi, x, t_p)/t_p$ as

$$\psi(\xi, t_p) \equiv \frac{1}{t_p}\left\langle \frac{\cos(\frac{\xi\omega}{t_p})}{\omega \sinh(\frac{\omega}{2t_p})}\right\rangle_{\rm ph}. \qquad (39)$$

For $t_p \ll 1$ and $t_p \gg 1$, $\psi(\xi, t_p)$ can be replaced by

$$\psi(\xi, t_p) \rightarrow \begin{cases} \psi(0, t_p)\tilde{\psi}(\xi), & t_p \ll 1, \\ \psi(0, t_p) - \tilde{F}(t_p)\xi^2, & t_p \gg 1, \end{cases} \qquad (40)$$

where

$$\tilde{\psi}(\xi) \equiv \lim_{t_p \to 0} \frac{\psi(\xi, t_p)}{\psi(0, t_p)} \qquad (41)$$

is computed numerically. It is a rapidly decaying function of $\xi$ and is negligibly small for $\xi \gtrsim 2$. The function $\tilde{F}(t_p) \equiv \langle \omega/[2t_p^3 \sinh(\omega/2t_p)]\rangle_{\rm ph}$ is computed numerically for $1 < t_p < 10^2$. Asymptotically, $\tilde{F}(t_p)$ has the form

$$\tilde{F}(t_p) = \begin{cases} 96\left(\frac{1}{a_1^3} + \frac{1}{a_2^3}\right)t_p, & t_p \lesssim 1, \\ \frac{1}{t_p^2}, & t_p \gtrsim 10^2. \end{cases} \qquad (42)$$

The function

$$\psi(0, t_p) = \left\langle \frac{1}{\omega t_p \sinh(\frac{\omega}{2t_p})}\right\rangle_{\rm ph} \qquad (43)$$

can be calculated numerically for a broad range of $t_p$ values, and can be shown to behave as

$$\psi(0, t_p) = \begin{cases} 2u_{-2} - \frac{1}{12t_p^2}, & t_p \gtrsim 1, \\ \pi^2\left(\frac{1}{a_1^3} + \frac{1}{a_2^3}\right)t_p, & t_p \lesssim 10^{-3}. \end{cases} \qquad (44)$$

With the aid of Eqs. (39)–(44), we can now derive low and high temperature limits of the effective structure factor $S_{\rm eff}$ of Eq. (37). For $t_p \ll 1$ one obtains

$$S_{\rm eff}(x, t_p) = 189\left(\frac{2}{\pi}\right)^5 e^{-2W(x,t_p)}G_{\rm eff}(xt_p\psi(0, t_p)), \qquad (45)$$

while for $t_p \gg 1$

$$S_{\rm eff}(x, t_p) = 189\left(\frac{2}{\pi}\right)^5 e^{-2W(x,t_p)+xt_p\psi(x,t_p)}$$
$$\times H_{\rm eff}(xt_pF(t_p)) - e^{-2W(x,t_p)}. \qquad (46)$$

Here we have defined

$$G_{\rm eff}(a) \equiv \int_0^\infty \frac{1 - 40\xi^2 + 80\xi^4}{(1 + 4\xi^2)^5\cosh^2(\pi\xi)} \times (e^{a\tilde{\psi}(\xi)} - 1), \qquad (47)$$

which obeys

$$G_{\rm eff}(a) \simeq \begin{cases} e^a, & a \gtrsim 10^2, \\ \frac{41\pi^5}{181440}a, & a \lesssim 0.1. \end{cases} \qquad (48)$$

For $0.1 \leq a \leq 10^2$ the value of $G_{\rm eff}$ is obtained numerically. The quantity $H_{\rm eff}$ in Eq. (46) is defined as

$$H_{\rm eff}(a) \equiv \int_0^\infty \frac{1 - 40\xi^2 + 80\xi^4}{(1 + 4\xi^2)^5\cosh^2(\pi\xi)} e^{-a\xi^2}. \qquad (49)$$

Asymptotically, $H_{\rm eff}$ behaves as

$$H_{\rm eff}(a) \simeq \begin{cases} \frac{1}{189}\left(\frac{\pi}{2}\right)^5 + 0.003690a, & a \lesssim 0.1, \\ (1/2)\pi^{1/2}a^{-1/2}, & a \gtrsim 10^3, \end{cases} \qquad (50)$$

but its values for $0.1 \leq a \leq 10^3$ need to be computed numerically.

To determine the contributions of the static lattice contribution (Bragg diffraction) to neutrino bremsstrahlung, we follow Ref. [20] who considered band structure effects. We begin with defining the dimensionless factor $L_{\rm sl}$,

$$L_{\rm sl} = \frac{1}{12Z_{\rm eff}}\sum_{\mathbf{K}\neq 0} \frac{1 - y_K^2}{y_K^2} \frac{|F(K)|^2}{|\epsilon(K)|^2} I(y, t_V)e^{-2W(y_K^2\tilde{\alpha}, t_p)}, \qquad (51)$$

where the sum is over $\mathbf{K}$ values below the electron Fermi surface, i.e., $y_K = K/(2k_F) < 1$ and $t_V = |V_{\mathbf{K}}|\sqrt{1 - y^2}/(k_BT)$ where $V_{\mathbf{K}}$ is given in Eq. (29). The integral $I(y, t_V)$ in Eq. (51) has been fitted analytically over a wide range of $t_V$ and $y$ values in Ref. [20].

In our case, which deals with a solid phase of rare phase blobs immersed in hadronic matter, the summation of $L_{\rm sl}$ sometimes consists only of a few terms. In the case of a bcc lattice, the condition for the summation to have at least $n$ terms (not counting multiplicity) is $y_{K_n} \leq 1$, which translates to a lower limit for $Z_{\rm eff} \geq Z_{\rm eff,min}^{(n)}$. The values of $Z_{\rm eff,min}^{(n)}$ for $n = 1$ through $n = 5$ are shown in Table IV.

Therefore, since $Z_{\rm eff} = Z$ in a lattice of nuclei immersed in an electron gas, $L_{\rm sl}$ is guaranteed to have a handful of terms. However, as we have seen in Sec. II C, the electron density will drop drastically with increasing baryon number density in the mixed phase region if $\chi \gtrsim 0.5$ so that $Z_{\rm eff}$ drops correspondingly (see Fig. 9 where the first few $Z_{\rm eff,min}^{(n)}$ are shown).

As will be shown in Sec. IV, for low temperatures of $T \lesssim 10^8 K$ and a quark volume fraction $\chi \gtrsim 0.5$ the summation consist only of a few terms, and the contribution of the static lattice oscillates vividly as a function of $\chi$ (see Figs. 11 and 12).

TABLE IV.   Lower bound values $Z_{\rm eff,min}^{(n)}$.

| $Z_{\rm eff,min}^{(1)}$ | $Z_{\rm eff,min}^{(2)}$ | $Z_{\rm eff,min}^{(3)}$ | $Z_{\rm eff,min}^{(4)}$ | $Z_{\rm eff,min}^{(5)}$ |
|---|---|---|---|---|
| $\sqrt{2}\pi/3$ | $4\pi/3$ | $\sqrt{6}\pi$ | $8\sqrt{2}\pi/3$ | $5\sqrt{10}\pi/3$ |

## C. Thermal conductivity

To calculate the thermal conductivity of quark-hybrid matter, we closely follow the formalism outlined in Ref. [21]. In general, the thermal conductivity of degenerate electrons is expressed in terms of an effective collision frequency $\nu_\kappa$ [43],

$$\kappa = \frac{\pi k_B^2 T n_e}{3 m_e^* \nu_\kappa}, \qquad (52)$$

which, in turn, can be expressed in terms of dimensionless Coulomb logarithms $\Lambda_\kappa$ [44],

$$\nu_\kappa^{ei} = \frac{4\pi Z^2 e^4 n_b}{p_F^2 v_F} \Lambda_\kappa, \qquad (53)$$

where $n_b$ is the number density of rare phase blobs in the mixed phase, and $p_F$ and $v_F$ are the Fermi momentum and Fermi velocity of relativistic electrons. For a solid phase, the Coulomb logarithms are calculated variationally in Born approximation [21,43],

$$\Lambda_{\kappa,\text{solid}} = \int_{y_0}^1 dy S_\kappa(y) \frac{|F(y)|^2}{y |\epsilon(y)|^2} \left(1 - \frac{x_r^2}{1 + x_r^2} y^2\right). \qquad (54)$$

Here, $x_r \equiv p_F/(m_e c)$ is a relativistic parameter and $y_0$, $F$, and $\epsilon$ have the same meaning as in Sec. III A. The quantity $S_\kappa$ stands for the effective static structure factor for thermal conductivity [21,42],

$$S_\kappa(y) = S_\sigma(y) + \left(\frac{3}{4y^2} - \frac{1}{2}\right) \delta S_\kappa(y), \qquad (55)$$

where $y = q/(2k_F)$ and $S_\sigma(y)$ are effective structure factors used to calculate the electric conductivity $\sigma$ [21].

Instead of using the asymptotic expressions and fitted formulas for $\Lambda_\kappa$ provided in Ref. [21], which cover $10^{-3} < t_p < 10$ and $0 < \tilde{\alpha} y^2 < 0.15$ [$\tilde{\alpha}$ is given by Eq. (32)], here we fully calculate their values and derive their asymptotic behaviors. This covers a wider range of $t_p$ and $\tilde{\alpha} y^2$ values. For this purpose, we rewrite the relevant integrals given in Refs. [21,42] in a form which is similar to $S_{\text{eff}}$ in Sec. III B, i.e.,

$$S_\sigma(y^2 \tilde{\alpha}, t_p) = \int_0^\infty d\xi \frac{\pi}{\cosh^2 \pi \xi} (e^{y^2 \tilde{\alpha} t_p \psi(\xi, t_p)} - 1)$$
$$\times e^{-2W(y^2 \tilde{\alpha}, t_p)},$$

$$\delta S_\kappa(y^2 \tilde{\alpha}, t_p) = \int_0^\infty d\xi \frac{2\pi(1 - 2\sinh^2 \pi \xi)}{\cosh^4 \pi \xi}$$
$$\times e^{-y^2 \tilde{\alpha} t_p \psi(\xi, t_p) - 2W(y^2 \tilde{\alpha}, t_p)}, \qquad (56)$$

where $\psi(\xi, t_p)$ denotes the phonon sum function already defined in Eq. (39). Since Bragg diffraction does not contribute to the thermal conductivity, there is no counterpart to $L_{\text{sl}}$.

Similar to Sec. III B, asymptotic expressions for $\psi(\xi, t_p)$ may be used to derive the high and low temperature limits for $S_\sigma$ and $\delta S_\kappa$. One then obtains

$$S_\sigma(x, t_p) \stackrel{t_p \ll 1}{\to} G_\sigma(x t_p \psi(0, t_p)) e^{-2W(x, t_p)}$$
$$\stackrel{t_p \gg 1}{\to} (e^{x t_p \psi(0, t_p)} H_\sigma(x t_p \tilde{F}(t_p)) - 1) e^{-2W(x, t_p)},$$

$$\delta S_\kappa(x, t_p) \stackrel{t_p \ll 1}{\to} G_{\delta\kappa}(x t_p \psi(0, t_p)) e^{-2W(x, t_p)}$$
$$\stackrel{t_p \gg 1}{\to} H_{\delta\kappa}(x t_p \tilde{F}(t_p)) e^{x t_p \psi(0, t_p) - 2W(x, t_p)}, \qquad (57)$$

where $\tilde{F}(t_p)$ is given in Sec. III B and the functions $G_{\sigma, \delta\kappa}$ and $H_{\sigma, \delta\kappa}$ are defined as

$$G_\sigma(a) \equiv \int_0^\infty d\xi \frac{\pi}{\cosh^2 \pi \xi} (e^{a\tilde{\psi}(\xi)} - 1), \qquad (58)$$

$$G_{\delta\kappa}(a) \equiv \int_0^\infty d\xi \frac{2\pi(1 - 2\sinh^2 \pi \xi)}{\cosh^4 \pi \xi} e^{a\tilde{\psi}(\xi)}, \qquad (59)$$

$$H_\sigma(a) \equiv \int_0^\infty d\xi \frac{\pi}{\cosh^2 \pi \xi} e^{-a\xi^2}, \qquad (60)$$

$$H_{\delta\kappa}(a) \equiv \int_0^\infty d\xi \frac{2\pi(1 - 2\sinh^2 \pi \xi)}{\cosh^4 \pi \xi} e^{-a\xi^2}. \qquad (61)$$

The quantity $\tilde{\psi}(t_p)$ is defined in Sec. III B. The asymptotic limits of Eqs. (58)–(61) are given by

$$
\begin{aligned}
G_\sigma(a) &\simeq \begin{cases} e^a, & a \gtrsim 10^2, \\ \frac{2}{3}a, & a \lesssim 0.1, \end{cases} \\
G_{\delta\kappa}(a) &\simeq \begin{cases} e^a, & a \gtrsim 10^3, \\ \frac{8}{15}a, & a \lesssim 10^{-2}, \end{cases} \\
H_\sigma(a) &\simeq \begin{cases} \frac{1}{2}\pi^{3/2}a^{-1/2}, & a \gtrsim 10^2, \\ 1 - \frac{a}{12}, & a \lesssim 0.1, \end{cases} \\
H_{\delta\kappa}(a) &\simeq \begin{cases} \pi^{3/2}a^{-1/2}, & a \gtrsim 10^3, \\ \frac{2a}{\pi^2}, & a \lesssim 10^{-2}. \end{cases}
\end{aligned}
\qquad (62)
$$

For $a$ values outside the ranges listed above the values of $H$ and $G$ were calculated numerically. Asymptotic approximations for $S_\sigma$ were used for $t_p \lesssim 10^{-2}$ and $t_p \gtrsim 1$. For $t_p$ values outside of these intervals the expression for $S_\sigma$ was computed numerically. The asymptotic approximations for $\delta S_\kappa$ are valid, and have been used for $t_p$ values in the intervals $t_p \lesssim 10^{-2}$ and $t_p \gtrsim 10$.

## D. Specific heat

The calculation of the specific heat is much simpler than the calculation of the neutrino emissivities and of the thermal conductivity, since the specific heat does not involve scattering processes. In terms of the phonon sum used in Secs. III B and III C, the specific heat density can be written as

$$c_{V,\text{solid}} = \hbar\omega n_b \frac{\partial}{\partial T}\left\langle\frac{3\omega}{\exp(\frac{\omega}{2t_p})-1}\right\rangle = \frac{3k_B n_b}{4t_p^2}\left\langle\frac{\omega^2}{\sinh^2(\frac{\omega}{2t_p})}\right\rangle.$$
(63)

The asymptotic low and high temperature expressions of Eq. (63) are given by

$$c_{V,\text{solid}} = \begin{cases} 3k_B n_b\left(1 - \frac{1}{36t_p^2}\right), & t_p \gtrsim 10^2, \\ 72k_B n_b\left(\frac{1}{a_1^3} + \frac{1}{a_2^3}\right)t_p^3, & t_p \lesssim 10^{-2}. \end{cases}$$
(64)

For temperatures greater than the melting temperature we adopt Eq. (24) of Ref. [45] for the specific heat density,

$$c_{V,\text{liq,gas}} = \begin{cases} \frac{3}{2}k_B n_b, & \Gamma \leq 1 \\ \frac{3}{2}k_B\left(1 + \frac{\log\Gamma}{\log\Gamma_m}\right), & 1 < \Gamma \leq \Gamma_m, \end{cases}$$
(65)

where we use $\Gamma_m = 172$ (as in Secs. III B and III C) instead of the outdated value $\Gamma_m = 150$ [45].

## IV. RESULTS AND DISCUSSION

### A. Contribution to the specific heat

In this paper, we have calculated the specific heat stemming from rare phase blobs immersed in hadronic matter for four different parameter sets (see Table III) and three different values ($\eta = 0.5, 1, 2$) for the surface tension of rare phase blobs. It is intriguing to compare these results with the heat capacities of the hadronic and quark matter phases weighted by their volume fractions. For this purpose we compute the specific heat of a Fermi gas of leptons and baryons from

$$c_V^l = \frac{k_B^3}{3\hbar^3}T\sqrt{m_l^2 + k_{F,l}^2}\,k_{F,l},$$
(66)

$$c_V^b = \frac{k_B^3}{3\hbar^3}T\sum_B m_B^* k_{F,B},$$
(67)

where $m_B^*$ is effective in-medium mass of baryons (see Sec. II). The specific heat of a quark gas is given by [46]

$$c_V^q = 0.6 \times 10^{20}\left(\frac{n_e}{\rho_0}\right)^{2/3}T_9 \text{ ergs cm}^{-3}\text{K}^{-1}.$$
(68)

The total specific heat of a mixture of quarks and hadrons follows from $c_V = (1-\chi)c_V^H + \chi c_V^Q$ where $c_V^H = c_V^b + c_V^l$ and $c_V^Q = c_V^q + c_V^l$. Figure 10 compares the different contributions to the specific heat with one another. As can be seen, the contribution of the rare phase blobs to the specific heat (colored lines in Fig. 10) is typically several orders of magnitude smaller than the specific heat of a standard (no geometrical structures) quark-hadron gas (solid black lines in Fig. 10). The small jumps at $\chi = 0.5$ in Fig. 10 are due to the discontinuity of the rare phase blob mass $m_b$ at $\chi = 0.5$ (see Fig. 7). The parameter sets HV2, G300I,
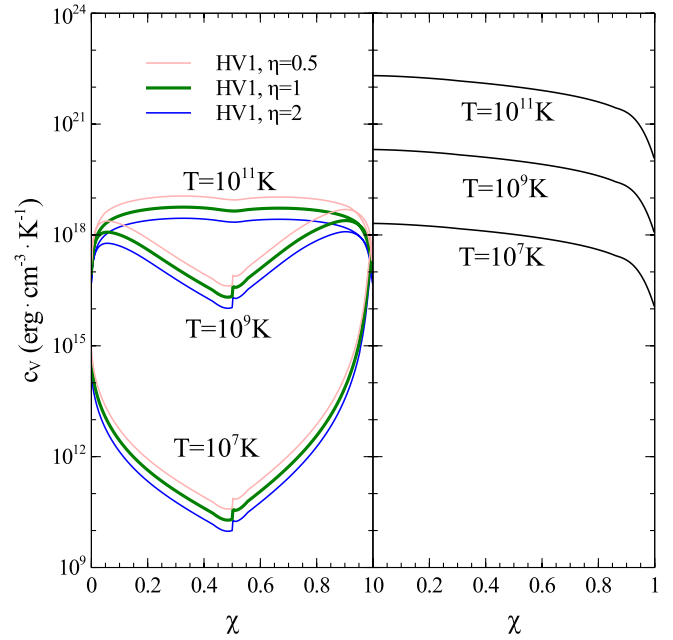


FIG. 10 (color online). Specific heat $c_V$ of mixed quark-hadron phase as a function of quark volume fraction $\chi$ computed for different surface tensions $\eta$ and temperatures $T$. The underlying equation of state is HV1. The panel on the left-hand side shows the contributions of the rare phase blobs to the specific heat. The curves in the panel on the right-hand side show the specific heat computed for a standard (no geometrical structures) quark-hadron gas.

and G300II lead to results very similar to those shown in Fig. 10 and are therefore not shown separately.

### B. Neutrino bremsstrahlung emissivity

The neutrino bremsstrahlung emissivities emerging from electron-phonon scattering and electron-lattice (Bragg diffraction) scattering have been computed from Eq. (33) for the four parameter sets of Table III. The surface tension of rare phase blobs in Eq. (24) has been varied again from $\eta = 0.5, 1,$ to 2. Figures 11 and 12 show the contributions of the rare phase blobs to the neutrino bremsstrahlung emissivity as a function of the quark volume fraction. A range of representative temperatures from $T = 10^7$ K to $10^{11}$ K has been chosen. For comparison, we show the contributions to the neutrino emissivity which comes from the modified URCA process in hadronic matter $\epsilon_{\nu,\text{H,MU}}$ and in quark matter $\epsilon_{\nu,\text{Q,MU}}$ [46]. Finally, we also show in these figures the emissivities which correspond to nucleon bremsstrahlung $\epsilon_{\nu,\text{H,BR}}$ and quark bremsstrahlung $\epsilon_{\nu,\text{Q,BR}}$ [9,46]. Their total contribution in quark-hybrid star matter is obtained for a given quark volume fraction $\chi$ from $\epsilon_\nu = \chi\epsilon_Q + (1-\chi)\epsilon_H$. As can be seen from Figs. 11 and 12, the neutrino emissivity from electron-blob bremsstrahlung becomes comparable to the emissivities of the modified URCA process (and other bremsstrahlung processes) for temperatures $T \lesssim 10^8$ K.
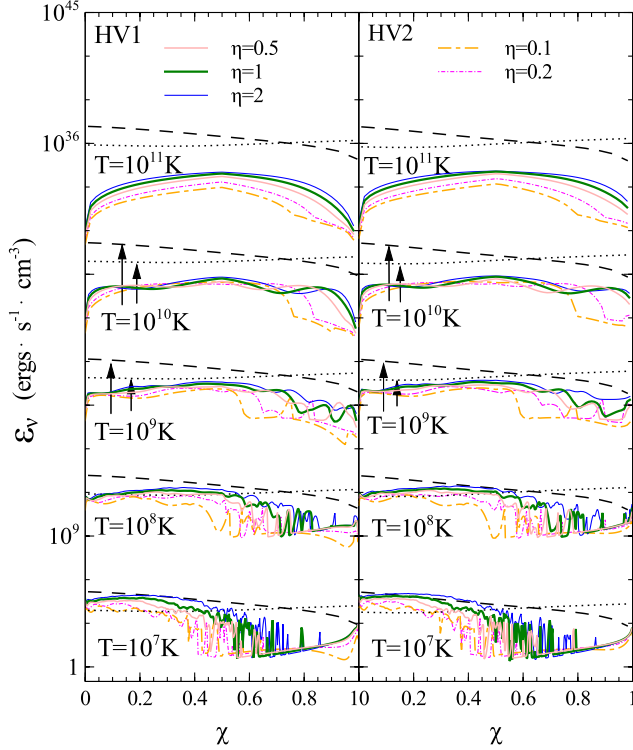
FIG. 11 (color online). Neutrino emissivities $\epsilon_\nu$ as a function of quark volume fraction $\chi$ at different temperatures computed for parameter sets HV1 and HV2. The colored lines show the total contributions from electron-blob bremsstrahlung for different surface tensions: $\eta = 0.1$ (orange dash-dot), $\eta = 0.2$ (thin pink dash-dot), $\eta = 0.5$ (light red), $\eta = 1$ (thick green), $\eta = 2$ (thin blue). The black lines show the total contributions from modified nucleon and quark URCA processes (dashed line) and nucleon-nucleon and quark-quark bremsstrahlung processes (dotted line).
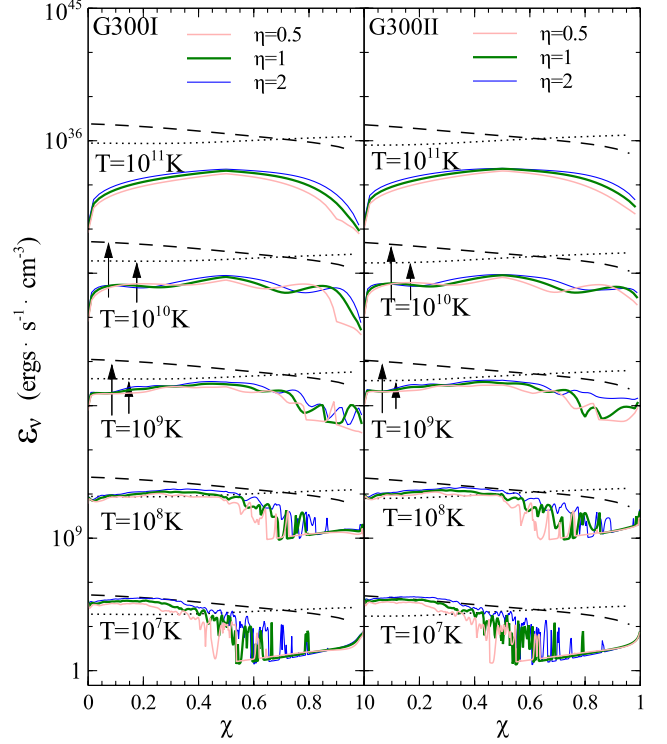
FIG. 12 (color online). Same as Fig. 11 but for parameter sets G300I and G300II. The colored lines show the total contributions from electron-blob bremsstrahlung for different surface tensions, $\eta = 0.5$ (light red), $\eta = 1$ (thick green), $\eta = 2$ (thin blue). (For the sake of clarity, the curves for $\eta = 0.1$ and $\eta = 0.2$ are not shown.) The black lines show the total contributions from modified nucleon and quark URCA processes (dashed line) and nucleon-nucleon and quark-quark bremsstrahlung processes (dotted line).

The bremsstrahlung emissivities oscillate rapidly with $\chi$ for $T \lesssim 10^9$ and $\chi \gtrsim 0.5$. This is due to Bragg diffraction given by the sum in the expression for $L_{sl}$ [see Eq. (51)]. As mentioned in Sec. III B, the sum of $L_{sl}$ consists only of a few terms if $\chi \gtrsim 0.5$. The oscillations are essentially due to the oscillating values of the individual terms in Eq. (51). The oscillations are smoothed out when the number of terms is large.

It also follows from Figs. 11 and 12 that the neutrino emissivity of rare phase blob bremsstrahlung at low temperatures but greater quark volume fractions ($\chi \gtrsim 0.5$) becomes sensitive to the choice of $\eta$. This feature, however, does not lead to large uncertainties in the total neutrino emissivity, since the neutrino emissivities for this temperature-density regime are dominated by the modified URCA process and nucleon-nucleon and quark-quark bremsstrahlung processes.

### C. Thermal conductivity

Figures 13–16 show the thermal conductivities due to presence of rare phase blobs. For comparison, thermal conductivities in standard quark-hadron gas are shown

too where the thermal conductivity for hadronic phase $\kappa_H$ is adopted from Ref. [47] and that of quark phase $\kappa_Q$ is adopted from Ref. [48]. The total thermal conductivity in standard quark-hadron gas without blobs is given by

$$\kappa = \left( \frac{\chi}{\kappa_Q} + \frac{1 - \chi}{\kappa_H} \right)^{-1}. \tag{69}$$

Besides scattering between electron and rare phase blobs calculated in Sec. III C, the geometric pattern will also alter the total thermal conductivity. The two contributions $\kappa_H$ and $\kappa_Q$ from standard quark-hadron gas can be combined using an expression for the total effective thermal conductivity of spheres immersed in continuous matter of a different thermal conductivity [49]. In our case the bulk thermal conductivity of two phases can be written as

$$\kappa_{eff} = \kappa_1 \left( 1 - \frac{3\chi}{(2\kappa_1 + \kappa_2)/(\kappa_1 - \kappa_2) + \chi} \right), \tag{70}$$

where $\kappa_1$ and $\kappa_2$ are the thermal conductivities of the dominant and the rare phase, respectively.
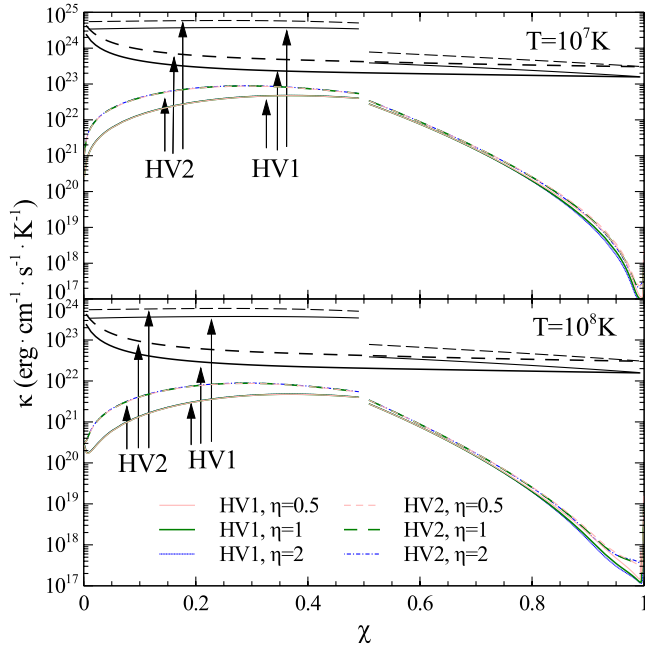
FIG. 13 (color online).   Thermal conductivity $\kappa$ as a function of quark volume fraction $\chi$ for matter at a temperature of $10^7$ K and $10^8$ K. The colored lines show the contributions of electron-blobs scattering in the mixed quark-hadron phase to $\kappa$ computed for parameter sets HV1 (solid) and HV2 (dashed) for different surface tensions [see Eq. (24)]: $\eta = 0.5$, 1, 2. The thick black lines show thermal conductivities of a standard (no blobs) quark-hadron gas computed for HV1 and HV2. The thin black lines show the effective bulk thermal conductivities defined in Eq. (70) in the presence of rare phase blobs embedded in dominant phase without contribution from electron-blob scattering for HV1 (dotted line) and HV2 (dash-dotted line).
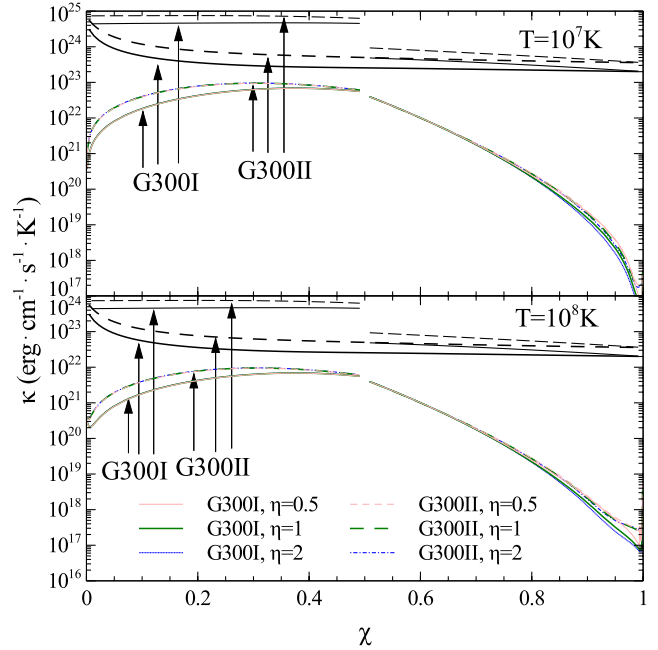


FIG. 15 (color online).   Thermal conductivity $\kappa$ as a function of quark volume fraction $\chi$ for matter at a temperature of $10^7$ K and $10^8$ K. The colored lines show the contributions of electron-blobs scattering in the mixed quark-hadron phase to $\kappa$ computed for parameter sets HV1 and HV2 for different surface tensions [see Eq. (24)]: $\eta = 0.5$, 1, 2. The thick black lines show thermal conductivities of a standard (no blobs) quark-hadron gas computed for G300I (solid) and G300II (dashed). The thin black lines show the effective bulk thermal conductivities defined in Eq. (70) in the presence of rare phase blobs embedded in dominant phase without contribution from electron-blob scattering for G300I (solid) and G300II (dashed).
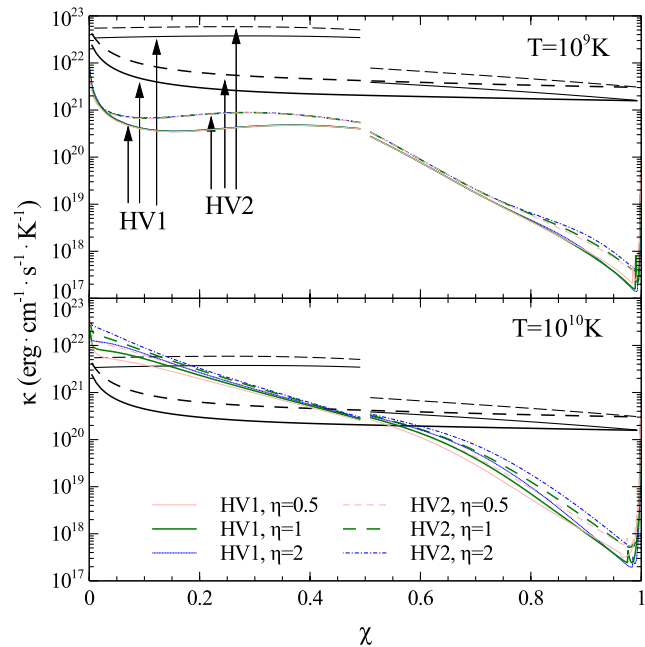


FIG. 14 (color online).   Same as Fig. 13 but for a temperature of $T = 10^9$ K and $10^{10}$ K.
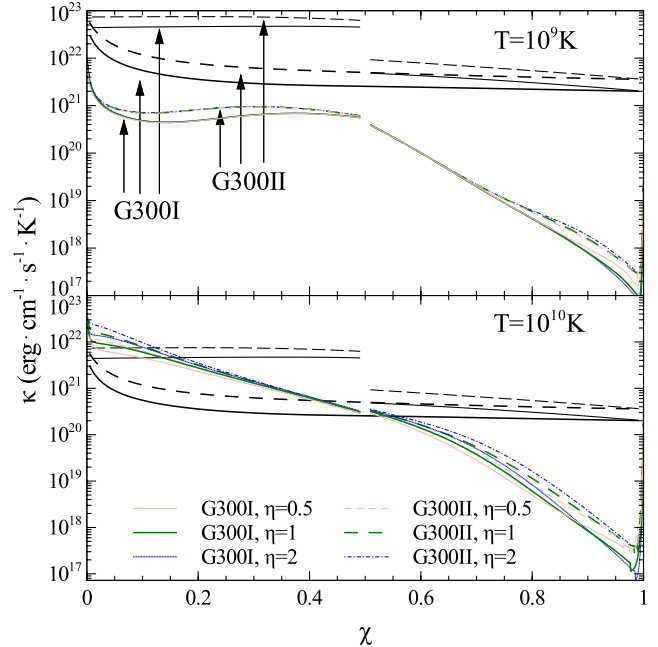


FIG. 16 (color online).   Same as Fig. 15 but for a temperature of $T = 10^9$ K and $10^{10}$ K.

The small jumps of thermal conductivities from electron-blob scattering (color lines in Figs. 13–16) are due to discontinuities of rare phase blob mass $m_b$ (See Fig. 7). The jumps of thermal conductivities contributed by embedding of rare phase blobs (thin black lines in Figs. 13–16) are due to unequal thermal conductivities of the two phases $\kappa_1 \neq \kappa_2$ at $\chi = 0.5$.

As can be seen from Figs. 13–16, the total thermal conductivity $\kappa = (\kappa_{\text{eff}}^{-1} + \kappa_{\text{blob}}^{-1})^{-1}$ is dominated by electron-blob scattering at $T \lesssim 10^9$ K. This is particularly the case for quark volume fractions close to $\chi = 0$ or $\chi = 1$ where the electron thermal conductivity from blob scattering can be as much as three (for $\chi < 0.5$) to six orders of magnitude ($\chi > 0.5$) smaller than the contribution from the mixed quark-hadron phase. Physically, this causes a blocking of the thermal flow through a mixed quark-hadron phase region, which could manifest itself in the thermal evolution of quark-hybrid stars.

As mentioned in Sec. II C, the blob volume density $n_b \to 0$ as $\chi \to 0$ or $\chi \to 1$. Since the Coulomb logarithm $\Lambda_\kappa$ is finite for these limits but the coefficient $\propto Z_{\text{eff}}$ is divergent, the thermal conductivity stemming from rare phase blob scattering will diverge on both ends of the quark-hadron phase leading to a vanishing total thermal conductivities there. Since this occurs only very near the edges of the quark-hadron boundary ($\chi \lesssim 10^{-2}$) this feature cannot be seen in Fig. 13. The small jumps in $\kappa$ near the edges of the quark-hadron phase for $T = 10^9$ K and $10^{10}$ K (see Figs. 14 and 16) are due to melting.

## V. SUMMARY AND CONCLUSIONS

Because of the competition between the Coulomb and the surface energies associated with the positively charged regions of nuclear matter and negatively charged regions of quark matter, the mixed phase may develop geometrical structures (e.g., blobs, rods, slabs) similarly to what is expected of the subnuclear liquid-gas phase transition. In this paper we explore the consequences of a Coulomb lattice made of rare phase blobs for the thermal and transport properties of neutron stars. The total specific heat $c_V$, thermal conductivity $\kappa$, and electron-blob bremsstrahlung neutrino emissivities $\epsilon_{\nu,\text{BR}}$ are calculated and compared with those of standard neutron star matter. To carry out this project, we have adopted and expanded on methods of earlier works on the transport properties of neutron stars [7,25]. The sizes of and spacings between rare phase blobs are calculated using the Wigner-Seitz approximation [7]. The equations of state used in this study are computed for a standard nonlinear nuclear Lagrangian, and the associated equations of motion for the baryon and meson fields are solved in the relativistic mean-field approximation. Quark matter has been modeled in the framework of the MIT bag model. Four different parameter sets (HV1, HV2, G300I, G300II) have been used to model the composition of neutron star matter containing a mixed phase of quarks and hadrons (quark-hybrid matter).

The results discussed in Sec. IV show that the contribution of rare phase blobs in the mixed phase to the specific heat is negligible compared to the specific heat of a quark-hadron gas. This is very different for the transport properties. For low temperature $T \lesssim 10^8$ K the neutrino emissivity from electron-blob bremsstrahlung scattering is at least as important as the total contribution from other bremsstrahlung processes (such as nucleon-nucleon and quark-quark bremsstrahlung) and modified nucleon and quark URCA processes (see Figs. 11 and 12). It is also worth noting that the scattering of degenerate electrons off rare phase blobs in the mixed phase region lowers the thermal conductivity by several orders of magnitude compared to a quark-hadron phase without geometric patterns (see Figs. 13–16). This may lead to significant changes in the thermal evolution of the neutron stars containing solid quark-hadron cores, which will be part of a future study. Another very interesting issue concerns the impact of more complex geometrical structures (rods and slabs) on the thermal conductivity and on neutrino transport. The presence of such structures may reduce the neutrino emissivities because of changes in the dimension of the reciprocal lattice and the Debye-Waller factor [20].

In summary, our study has shown that the presence of rare phase blobs in dense neutron star matter may have very important consequences for the total neutrino emissivity and thermal conductivity of such matter. The implications of this for the thermal evolution of neutron stars need to be explored in future studies. To accomplish this we intend on performing two-dimensional cooling simulations in which rotation and a dynamic composition might be accounted for Refs. [50,51]. In this connection we refer to the recent study of Noda *et al.* [52], who suggested that the rapid cooling of the neutron star in Cassiopeia A can be explained by the existence of a mixed quark-hadron phase in the center of this object.

[1] D. D. Ivanenko and D. F. Kurdgelaidze, Astrophys. J. **1**, 251 (1965).

[2] H. Fritzsch, M. Gell-Mann, and H. Leutwyler, Phys. Lett. **47B**, 365 (1973).

[3] G. Baym and S. Chin, Phys. Lett. **62B**, 241 (1976).

[4] B. D. Keister and L. S. Kisslinger, Phys. Lett. **64B**, 117 (1976).

[5] G. Chapline and M. Nauenberg, Phys. Rev. D **16**, 450 (1977); Ann. N.Y. Acad. Sci. **302**, 191 (1977).

[6] W. B. Fechner and P. C. Joss, Nature (London) **274**, 347 (1978).

[7] N. K. Glendenning, Phys. Rep. **342**, 393 (2001).

[8] N. K. Glendenning, *Compact Stars, Nuclear Physics, Particle Physics, and General Relativity* (Springer-Verlag, New York, 2000), 2nd ed.

[9] F. Weber, *Pulsars as Astrophysical Laboratories for Nuclear and Particle Physics*, Studies in High Energy Physics Cosmology and Gravitation (Institute of Physics Publishing, Bristol, 1999).

[10] F. Weber, Prog. Part. Nucl. Phys. **54**, 193 (2005).

[11] T. Maruyama, S. Chiba, H.-J. Schulze, and T. Tatsumi, Phys. Rev. D **76**, 123015 (2007).

[12] N. K. Glendenning, Phys. Rev. D **46**, 1274 (1992).

[13] D. G. Ravenhall, C. J. Pethick, and J. R. Wilson, Phys. Rev. Lett. **50**, 2066 (1983).

[14] D. G. Ravenhall, C. J. Pethick, and J. M. Lattimer, Nucl. Phys. **A407**, 571 (1983).

[15] R. D. Williams and S. E. Koonin, Nucl. Phys. **A435**, 844 (1985).

[16] N. K. Glendenning and S. Pei, Phys. Rev. C **52**, 2250 (1995).

[17] N. K. Glendenning, Phys. Rep. **342**, 393 (2001).

[18] H. Heiselberg, C. J. Pethick, and E. F. Staubo, Phys. Rev. Lett. **70**, 1355 (1993).

[19] H. Heiselberg, in *Proceedings of the International Symposium on Strangeness and Quark Matter*, edited by G. Vassiliadis, A. D. Panagiotou, B. S. Kumar, and J. Madsen (World Scientific, Singapore, 1995), p. 298.

[20] A. D. Kaminker, C. J. Pethick, A. Y. Potekhin, V. Thorsson, and D. G. Yakovlev, Astron. Astrophys. **343**, 1009 (1999).

[21] A. Y. Potekhin, D. A. Baiko, P. Haensel, and D. G. Yakovlev, Astron. Astrophys. **346**, 345 (1999).

[22] R. Mochkovitch and J. P. Hansen, Phys. Lett. **73A**, 35 (1979).

[23] N. K. Glendenning, Astrophys. J. **293**, 470 (1985).

[24] F. Weber and M. K. Weigel, Nucl. Phys. **A505**, 779 (1989).

[25] N. K. Glendenning, Nucl. Phys. **A493**, 521 (1989).

[26] A. Chodos, R. L. Jaffe, K. Johnson, C. B. Thorne, and V. F. Weisskopf, Phys. Rev. D **9**, 3471 (1974).

[27] A. Chodos, R. L. Jaffe, K. Johnson, C. B. Thorne, and V. F. Weisskopf, Phys. Rev. D **10**, 2599 (1974).

[28] E. Farhi and R. L. Jaffe, Phys. Rev. D **30**, 2379 (1984).

[29] G. Baym, C. J. Pethick, and P. Sutherland, Astrophys. J. **170**, 299 (1971).

[30] P. B. Demorest, T. Pennucci, S. M. Ransom, M. S. E. Roberts, and J. W. T. Hessels, Nature (London) **467**, 1081 (2010).

[31] M. Orsaria, H. Rodrigues, G. A. Contrera, and F. Weber, Quark-Hybrid Stars in the Framework of the Nonlocal SU(3) Nambu-Jona Lasinio Model, SDSU, 2012 (to be published).

[32] W. D. Myers, W. J. Swiatecki, and C. S. Wang, Nucl. Phys. **A436**, 185 (1985).

[33] H. Nagara, Y. Nagata, and T. Nakamura, Phys. Rev. A **36**, 1859 (1987).

[34] B. Jancovici, Nuovo Cimento A **25**, 428 (1962).

[35] E. L. Pollock and J. P. Hansen, Phys. Rev. A **8**, 3110 (1973).

[36] D. A. Baiko and D. G. Yakovlev, Astron. Lett. **21**, 702 (1995).

[37] P. Haensel, A. D. Kaminker, and D. G. Yakovlev, Astron. Astrophys. **314**, 328 (1996).

[38] G. G. Festa and M. A. Ruderman, Phys. Rev. **180**, 1227 (1969).

[39] D. G. Yakovlev and A. D. Kaminker, Astron. Lett. **22**, 491 (1996).

[40] N. Itoh, S. Mitake, H. Iyetomi, and S. Ichimaru, Astrophys. J. **273**, 774 (1983).

[41] D. A. Young, E. M. Corey, and H. E. DeWitt, Phys. Rev. A **44**, 6508 (1991).

[42] D. A. Baiko, A. D. Kaminker, A. Y. Potekhin, and D. G. Yakovlev, Phys. Rev. Lett. **81**, 5556 (1998).

[43] J. M. Ziman, *Electrons and Phonons* (Oxford University Press, Oxford, 1960).

[44] D. G. Yakovlev and V. A. Urpin, Sov. Astron. **24**, 425 (1980).

[45] K. A. van Riper, Astrophys. J. **75**, 449 (1991).

[46] N. Iwamoto, Ann. Phys. (Berlin) **141**, 1 (1982).

[47] E. Flowers and N. Itoh, Astrophys. J. **250**, 750 (1981).

[48] P. Haensel, CAMK Report No. 228, 1991 (to be published).

[49] R. B. Bird, W. E. Stewart, and E. N. Lightfoot, *Transport Phenomena* (John Wiley & Sons, New York, 2002), 2nd ed.

[50] V. Dexheimer, R. Negreiros, and S. Schramm, arXiv:1108.4479.

[51] R. Negreiros, S. Schramm, and F. Weber, Phys. Rev. D **85**, 104019 (2012).

[52] T. Noda, M. Hashimoto, Y. Matsuo, N. Yasutake, T. Maruyama, T. Tatsumi, and M. Fujimoto, arXiv:1109.1080v1.